Accepted Manuscript

Wear mapping of CoCrMo alloy in simulated bio-tribocorrosion conditions of a hip prosthesis bearing in calf serum solution

K. Sadiq[a, b]*, M.M. Stack[a], R.A. Black[b]

[a] Department of Mechanical Engineering, University of Strathclyde, 75 Montrose St., Glasgow, G1 1XJ, UK

[b] Department of Biomedical Engineering, University of Strathclyde, Wolfson Centre, 106 Rottenrow, Glasgow, G4 0NW, UK

* Corresponding author K. Sadiq

Tel.: +44 141 574 5079

e-mail address: kamran.sadiq@strath.ac.uk (K. Sadiq)

Abstract

Wear maps were developed following a series of micro-abrasion–corrosion testing during idealised hip contact conditions for a CoCrMo alloy in a foetal calf serum solution. The main aim of the study was to characterise wear–corrosion or bio-tribocorrosion regimes of the alloy over a range of applied loads and applied potentials. The transitioning micro-abrasion–corrosion mechanisms, synergisms and wastage behaviours in the presence of additional abrasive particles were identified and mapped. Wear maps in earlier work show the wear–corrosion transitions of CoCrMo alloy in the absence of abrasive particles for similar conditions; the wear maps developed in this work were compared. Mapping the micro-abrasion–corrosion regimes indicated that proteins present in foetal calf serum solution, resulting in development of a graphitic tribo-layer, may play a critical role in enhancing or protecting against tribo-corrosive degradation.

Keywords

Bio-tribocorrosion
CoCrMo
Hip replacement
Calf serum
Tribocorrosion maps
Wear mapping

1 Introduction

According to the 2013 UK National Joint Registry (1) there were 76,448 primary hip and 10,040 revision procedures performed for 2011/2012 in England and Wales. The number of joint replacements is expected to increase as the ageing population grows. Revision procedures continue to increase in number due to aseptic loosening, osteolysis, infection, recurrent dislocation, malalignment, and implant failure or fracture. Wear is widely recognized as the primary mode of failure and limiting factor in the long-term stability of hip joint replacements (2, 3). A fundamental understanding of the tribology and corrosion mechanisms is therefore critical in developing safe, reliable and long-lasting hip replacements. In the present study wear maps have been developed relating the micro-abrasion and corrosion behaviours and transitions of a cobalt–chromium–molybdenum (CoCrMo) versus ultra-high molecular weight polyethylene (UHMWPE) hip bearing contact in a calf serum solution and in the presence of abrasive particles.

The study of bio-tribocorrosion, i.e. tribology (friction, wear, lubrication) and corrosion occurring simultaneously in a biological environment is still an emerging and developing field of research (4). Tribocorrosion is an irreversible transformation of a material as a result of simultaneous physicochemical and mechanical surface interactions occurring in a tribological contact (5). The total material loss in a tribocorrosion system is not simply the sum of losses due to the mechanical and corrosion wear components alone (4, 5). Corrosion and wear are significantly modified during the tribocorrosion interactions exhibiting a synergism or antagonism effect that may result in accelerated or reduced mass loss.

The clinical implications of wear in hip replacements are well documented (2, 3, 6). Recently unprecedented high clinical failure rates have been reported for metal-on-metal hip replacement (7) with serious ramifications for patients, healthcare providers and orthopaedic manufacturers . There is an urgent need to comprehensively understand the underlying wear mechanisms occurring hip replacements (e.g. total hip replacement) from a tribocorrosion perspective (4, 7, 8). As wear is commenced in a hip bearing contact, it can alter the tolerances between the ball and cup. As a result this may alter the biomechanics, function and range of hip motion, bearing impingement, subluxation or joint dislocation. Wear may also transform the bearing surface properties physically and chemically, including coatings. Wear particles and wear debris generated as by-products of wear can cause adverse local and systemic reactions on the host leading to tissue inflammation surrounding the joint, osteolysis, implant loosening or fracture. Buford and Goswami (6) described the wear mechanisms in hip replacement as a function of the material type, contact stresses, lubricants and clearance, surface hardness and roughness, type of articulation due to motion, cycles, solution particle count and distribution, and oxidative wear.

Detailed literature on the history and development of wear mapping is available (9). It is widely accepted that the investigation of wear in a comprehensive and systematic manner is complex. There are many independent variables involved in a wear system. These can be divided into continuous (i.e. speed, load, temperature) and discrete (i.e. dry, aqueous, lubricant, environment) to name a few; the concept of wear maps can be utilized to

classify these many variables (9, 10). The complete wear behaviour for a given material combination can be systematically defined by mapping a series of three-dimensional wear maps as a function of a fixed discrete variable. For example wear vs. speed and load; wear vs. speed and temperature; and wear vs. speed and time for a given material may be assessed under dry sliding, in non-reactive fluid (temperature control at the contact interface), and in a reactive lubricant (9). In this way a series of wear maps can be constructed for a given material couple describing the wear behaviour. Though it is not always necessary to construct a complete set of such maps, a selection of maps defining the critical limits and operational boundaries for the desired range of wear parameters may be utilized. Further it is accepted that it is not sufficient to describe or predict wear behaviour for a given material couple by a single wear model (9), for the different operational and environmental conditions separate wear models are required and this becomes graphically apparent by means of wear mapping. Lim and Ashby (11) demonstrated the construction of wear mechanism maps as early as 1987. Such mapping approaches can be used to evaluate, predict and optimize the wear behaviours of a given material couple for any given mode of operation (9, 10).

Wear mapping may aid in solving tribocorrosion related problems for industrial and biomedical engineering applications. Some progress has been made in constructing wear maps for hip replacements (12, 13). In other work, significant wear selection maps for biological materials have also been constructed (14). Defining and mapping the wear–corrosion and wear parameters for materials that are clinically relevant, in physiological

5

conditions may aid in evaluating a host of biomedical implantable devices. In this way long-term performance and patient health outcomes may be predicted and optimized.

In micro-scale abrasion testing a rotating ball is pressed into the surface of a test sample in the presence of an abrasive solution, the schematic diagram is shown in Fig. 1. A spherical crater or scar is generated as a result of material wear on the sample surface. Wear performances may be evaluated by comparing wear scar sizes for different materials, the scar is commonly measured using optical microscopy. Micro-scale abrasion testing is relatively low-cost; small material samples are required and rapid tests may be conducted. These are some of the advantages micro-scale abrasion testing has over other and more well-established tribological methods. A comprehensive review of micro-scale abrasion testing is provided in the literature (15). There are two modes of wear generally observed in micro-scale abrasion testing: grooving (two-body) abrasion and rolling (three-body) abrasion. Two-body abrasion is identified as a series of fine parallel grooves in the scar surface, whereas multiple indentations and no distinct directional groove lines in the scar surface are characteristic of three-body abrasion. The dominant wear mode is a function of several factors including applied load, volume fraction of abrasion particles and the material types (ball and sample). Adachi and Hutchings (16) developed wear mode maps to identify the transitions from two- to three-body abrasion regimes for different material and test conditions. Stack and Mathew (17) further developed micro-abrasion mechanism maps defining the micro-abrasion transition regimes over the two-body and three-body regimes and demonstrating the complexity of the wear mechanisms for several metallic materials. In total hip and knee replacements the third-body particle

may be either poly(methyl methacrylate) PMMA in the case of a cemented prosthesis, or carbides originating in the bearing surface (3). In some cases bone debris generated during surgical implantation may become trapped in the articulating bearing and act as third-body particle.

Wear maps have been developed for simulated hip contact conditions using CoCrMo alloy in Ringer's solution during micro-scale abrasion conditions by the current research group (12). The simultaneous micro-abrasion and corrosion behaviours were assessed in a modified micro-scale abrasion tester and potentiostat. The micro-abrasion–corrosion (MAC) material wastage, abrasion mechanisms, and wear–corrosion synergisms were defined and mapped. In more recent work by the same group further wear maps were developed for CoCrMo alloy in a calf serum solution (13). The presence of protein has been shown to play a significant role in hip wear as a potential protective mechanism (18). The aim of this work was to characterise the wear–corrosion regimes of CoCrMo alloy and UHMWPE couple over a range of applied loading and applied potentials in a calf serum solution and in the presence of abrasive particles. The transitioning MAC mechanisms, synergisms and wastage behaviours of CoCrMo alloy have been identified and mapped. A comparison of the wear maps in protein solution with and without the addition of abrasive particles is presented.

2 Materials and methods

2.1 Materials

Test samples were pre-machined from a low-carbon CoCrMo wrought alloy rod stock (ATI Allvac, USA). The elemental composition of the alloy corresponds to ASTM F-1537 (wt.%: C 0.03%, Cr 27.56%, Mo 5.70%, Mn 0.60%, Si 0.38%, Al<0.02% and Co 64.96%). The samples were supplied in the form of disks each 29 mm in diameter and 4 mm thick. Prior to testing the alloy surfaces were ground with SiC paper up to 2000 grit and then progressively polished using 6 then 3 μm diamond pastes. Thereafter the sample was finished with a final polish to a mirror finish using a 0.05 μm colloidal silica paste (Struers Ltd., UK). The resulting surfaces were polished to a mirror finish and a roughness (R_a) of 0.012 μm. The surface roughness was measured using an MFP-3D Atomic Force Microscope (Asylum Research, USA) in contact mode and with an Olympus AC-160 cantilever tip. The samples were cleaned in ethanol and rinsed using distilled water, then allowed to dry in air before assembling into the rig for testing. The counter-face material was an ultra-high molecular weight polyethylene (UHMWPE) (K-mac Plastics, USA) 25 mm diameter ball. The maximum surface roughness of the ball was 0.02 μm (according to the manufacturer). The CoCrMo and UHMWPE material properties are shown in Table 1.

A base solution of 0.9 wt.% sodium chloride (NaCl) (Sigma-Aldrich, UK), and 10 vol.% foetal calf serum (FCS) (Biosera, UK) was used for the electrolyte. NaCl represents a simple simulated biological fluid and contains a similar level of chloride to human bodily

fluids; the addition of FCS was used as an analogue for synovial fluid; also a commonly used medium in wear test apparatus to evaluate the effect of protein during micro-abrasion–corrosion. The pH of this solution was 7.3, and remained constant for the duration of the test. The electrolyte solution was refrigerated and used within 24 h of preparation; the temperature during testing was kept at around 25°C. The solution was supplemented with F-1200 grade black silicon carbide particles (UKGE Ltd., UK) to a final concentration of 0.025 g ml^{-1} to represent the presence of third-body particles. The abrasive particle grains were angular shaped with Mohs hardness between 9 and 10. The average particle size was 3 μm.

	Material	Diameter (mm)	Density (kg/m^3)	Vickers Hardness	Young's modulus (GPa)	Poisson's Ratio
Specimen	Wrought CoCrMo alloy	–	8300	390 HV max	248	0.3
Ball	UHMWPE	25.0	931–935	8.3 HV max	0.94	0.46

Table 1: Properties of materials used for ball and specimen

2.2 Experimental procedures

2.2.1 Micro-abrasion–corrosion apparatus

The apparatus, shown schematically in Fig. 1, consisted of a micro-abrasion tester (Plint TE-66, Phoenix Tribology) and an integrated Gill AC potentiostat (ACM Instruments, UK). A UHMWPE ball was fixed between two co-axial shafts carried by support bearings. The ball was rotated uni-directionally by a variable speed DC motor via a single shaft. Shaft revolutions were counted with an in-built batch counter. Electrolyte solution

9

was fed to a point closely above the sample-ball contact, delivered by a peristaltic pump from a separate glass container kept at 25°C room temperature. The sample surface was insulated with a non-conductive polyethylene coating; a surface area of 1 cm^2 was kept exposed for wear testing. In order to generate wear scars the sample was clamped on to a platform located on a pivoting L-shaped arm. The arm could be rotated on a pivot and the sample pressed on the ball. Load was applied by adding dead weights to a cantilever arm. The same sample was abraded multiple times by moving the L-shaped arm horizontally to a fresh site. A small automatic stirrer rotating at approximately 1000 rpm was used in the solution feed container to ensure an evenly mixed solution of suspended abrasive particles.
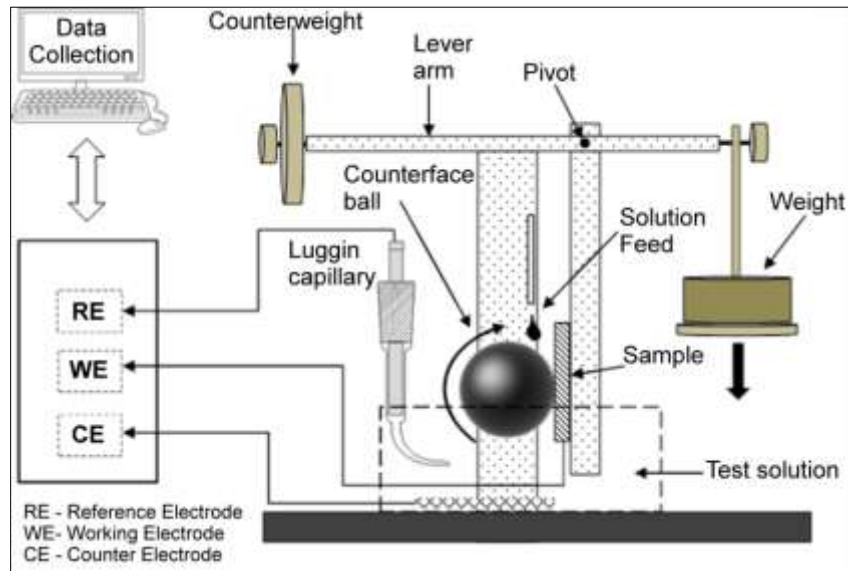
Figure 1: Schematic diagram of the micro-abrasion–corrosion apparatus

2.2.2 Electrochemical tests

Two types of electrochemical tests were conducted for this study, potentiodynamic polarisation curves and potentiostatic tests. All measurements were recorded using a Gill AC potentiostat (ACM Instruments, UK). A three-electrode electrochemical setup consisted of a Platinum–Titanium (Pt–Ti) wire mesh counter electrode and a saturated calomel reference electrode (SCE) linked by a capillary tube immersed in the electrolyte solution proximal to the sample-ball contact. The sample was connected as the working electrode to complete the setup. Electrolyte solution was kept at room temperature (~25°C) and poured into the inert solution container; fresh solution was pumped from a separate container and fed to the sample-ball contact point. Prior to each test the samples were immersed in the testing solution for 10 min to stabilize the alloy surface. The polarisation sweep started at a cathodic potential of −1500 mV and moved in the anodic direction to 1500 mV at a sweep rate of 1.38 mV s^{-1}. The ball was rotated at 100 rpm (0.13 m s^{-1}) uni-directionally against the sample during polarisation measurements for duration of 30 min; equivalent to a total sliding distance of 235.50 m. Testing was repeated for increasing applied loads using a fresh electrolyte solution on freshly polished sample surface. It should be noted that all experiments were carried out at room temperature and the solution was exposed to air. The corrosion potential E_{corr} as well as the corrosion current density i_{corr} were determined from the polarisation curves by extrapolating Tafel slopes using dedicated potentiostat software, ACM Instruments version 5 (ACM Instruments, UK).

Potentiostatic tests were carried out for a range of applied potentials to determine the changes in mass (i.e., mass loss) and also to assess the corrosion behaviour (K_c) contributing to the total mass loss at increasing applied loads (n = 5). Resulting wear scars were analysed to determine the total mass loss (K_{ac}) once tests were complete. To determine the abrasion mass loss (K_a) in the absence of corrosion potentiostatic testing was conducted under cathodic conditions (–960 mV). A total of 25 potentiostatic tests were carried out over the testing parameter range in addition to the polarisation sweeps. A summary of the testing conditions and parameters is given in Table 2.

Applied loads (N)	0.5, 1, 2, 3 and 5
Applied potentials (SCE) (mV)	– 600, – 400, – 200, 0 and +200
Ball speed (rpm)	100
Total sliding distance (m)	235.50
Testing duration (s)	1800

Table 2: Micro-abrasion–corrosion test conditions

2.2.3 SEM analysis

The samples were carefully removed from the MAC apparatus once testing was complete. Loosely attached material was removed from the sample surface by rinsing in distilled water and the samples were then dried in air. A tungsten filament SEM (Hitachi S-3700) was used to acquire the surface topography images and to measure the resulting wear scar diameters. The mass loss volumes were estimated using a standard technique for measuring wear scar of spherical geometry (15). It is assumed the shape of the crater

conforms to the shape of the ball. The wear volume *(V)* may then be calculated by measurement of the crater diameter *(b)* and R the ball radius (for $b \ll R$) as shown in Eq. 1.

$$V \approx \frac{\pi b^4}{64R} \quad \text{For } b \ll R \tag{1}$$

Optical focus variation microscopy (InfiniteFocus G4, Alicona, Austria) was also used to acquire 3D wear scar information. The objective used was 20x giving a vertical resolution of 50 nm and minimum measurable roughness (Ra) of 0.15 µm. Due to the highly reflective surface of CoCrMo alloy it is difficult to acquire direct images using the optical instrument. Replications of the wear scars were made using special silicone resin supplied by the manufacturer (Alicona, Austria). Images were then acquired of the replications.

2.2.4 Energy dispersive X-ray analysis

Energy dispersive X-ray spectrometry analysis was introduced to evaluate the elemental compositions of the CoCrMo alloy worn and unworn surfaces; and to confirm the presence of organic material on the wear scar surfaces following testing. Proteins mainly consist of hydrogen, carbon, nitrogen and oxygen. Carbon compounds likely to be present as laboratory contaminants can be detected using EDS. Typically this is observed as a peak near 0.28 keV on examining the EDS spectrum. In contrast, it is much less likely to observe a nitrogen peak close to 0.39 keV in a typical EDS spectrum, due to random laboratory contamination; in the present work observation of a nitrogen peak

therefore can be attributed to the presence of protein. Oxford Inca EDS system (Model 350, Oxford Instruments, High Wycombe, UK) and built-in software was used to capture EDS spectra of different regions of worn and unworn sample surfaces between 5 and 8 keV.

3 Results

3.1 SEM and EDS Analysis

Typical SEM micrographs of wear scars are shown (Fig. 2). Wear scar diameters were measured in order to estimate the total mass loss as described in Eq. 1. Images of the scars generated in particle solution generally indicate a mixed abrasion mode (Figs. 2a and 2c); deep parallel groove towards the centre suggests two-body abrasion and towards the outer area there is indication of three-body abrasion where the grooves are not visibly distinct.
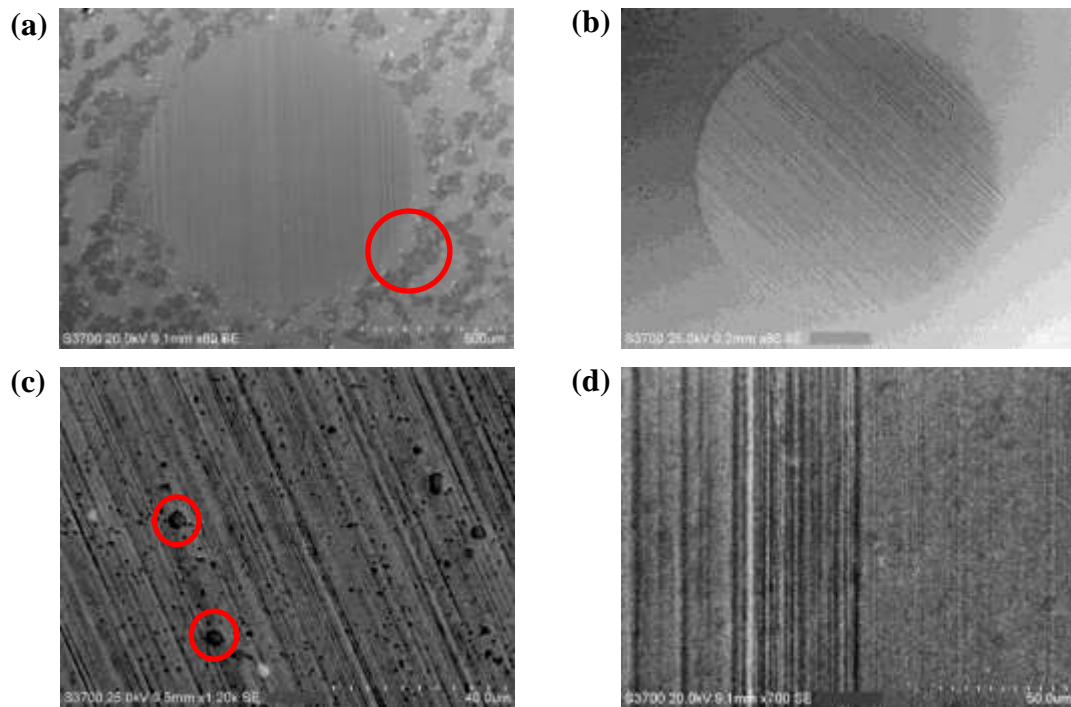
Figure 2: SEM micrographs of typical wear scar surfaces generated during micro-abrasion testing for CoCrMo alloy in FCS and 0.9 % NaCl solution: (a, c) in the presence of abrasive SiC particles deep parallel grooves are observed and tending towards a 3-body regime towards the outer periphery; agglomerated islands appear around the wear scar (circled red), (c) fine SiC particles appear embedded across wear surface including larger agglomerated particles (circled in red), (b, d) in the absence of abrasive particles a uniform 2-body abrasion is observed, (d) deep parallel grooves indicative of 2-body abrasion regime. Larger agglomerated particles are not observed.

Wear scars generated in non-particle solution however indicated a uniform dominant two-body abrasion (Figs. 2b and 2d). In the case of additional abrasive particles the surrounding surface of the scar shows formation of a surface film (circled red in Fig. 2a) observed as islands; likely to be composed of protein and SiC particles.
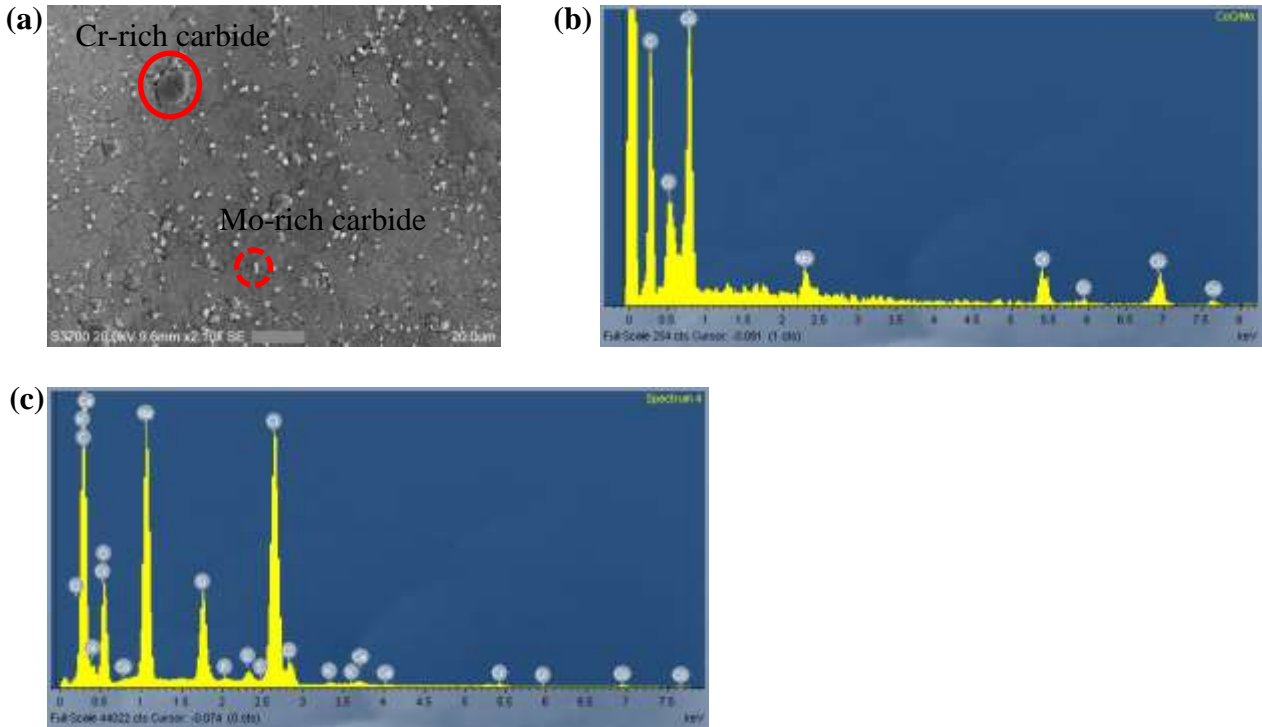
Figure 3: (a) SEM micrograph of polished and unworn CoCrMo alloy (ASTM F-1537), Cr-rich carbides (red circle) and Mo-rich (red dashed circle) clearly visible precipitating at Co rich grain boundaries, (b) typical EDS spectra of the unworn polished CoCrMo alloy surface indicating expected elemental composition. Carbon peak is observed at around 0.28 keV and may be attributed to laboratory contaminants. (c) EDS spectra for a typical wear scar surface generated in NaCl and FCS solution and in the presence of abrasive SiC particles. The presence of organic elements is clearly indicated, a nitrogen peak appears at around 0.39 keV in addition to high levels of C, Na and Cl. The Si peak at around 1.8 keV corresponds to the presence of SiC abrasive particle in the test solution.

SEM analysis of the unworn sample surface (Fig. 3a) reveals expected microstructural features according to ASTM F-1537. Precipitated Cr-rich and Mo-rich carbides are clearly observed scattered about the Co-rich grain boundaries. EDS spectra indicate expected elemental composition of the CoCrMo alloy close to the manufacturer

specification described earlier; typical spectra for clean and unworn surface is shown (Fig. 3b). EDS analysis for worn sample surfaces consists mainly of C in addition to Na, Cl, K, Ca, P, and O (Fig. 3c). Comparing the EDS spectra for the worn against clean unworn surfaces a nitrogen peak is observed at around 0.39 keV, clearly not visible on control samples. Additionally the C peak is increased significantly following testing on the worn sample surface in the region of 0.3 keV. The carbon and nitrogen peaks detected using EDS are good indicators of organic material present on the worn alloy surface; this is likely composed of proteins which appear to agglomerate more heavily around the scar diameter.

3.2 Optical focus-variation microscopy

An optical focus-variation microscopy analysis of the wear scars indicated a mixed-mode abrasion regime for the particle solution, which corresponds to the SEM analysis. Fig. 4 shows typical wear scar profiles produced by the different test solutions. While the size and depth of the wear scars varied according to the test conditions, in all cases the wear scars conform to a hemispherical shape consistent with the analysis carried out in the previous section. While the 2D profiles illustrated in Fig. 4 do show some difference in terms of roughness for the different solutions, those differences may be accounted for by the presence of particles.

(a)

(b)

(c)
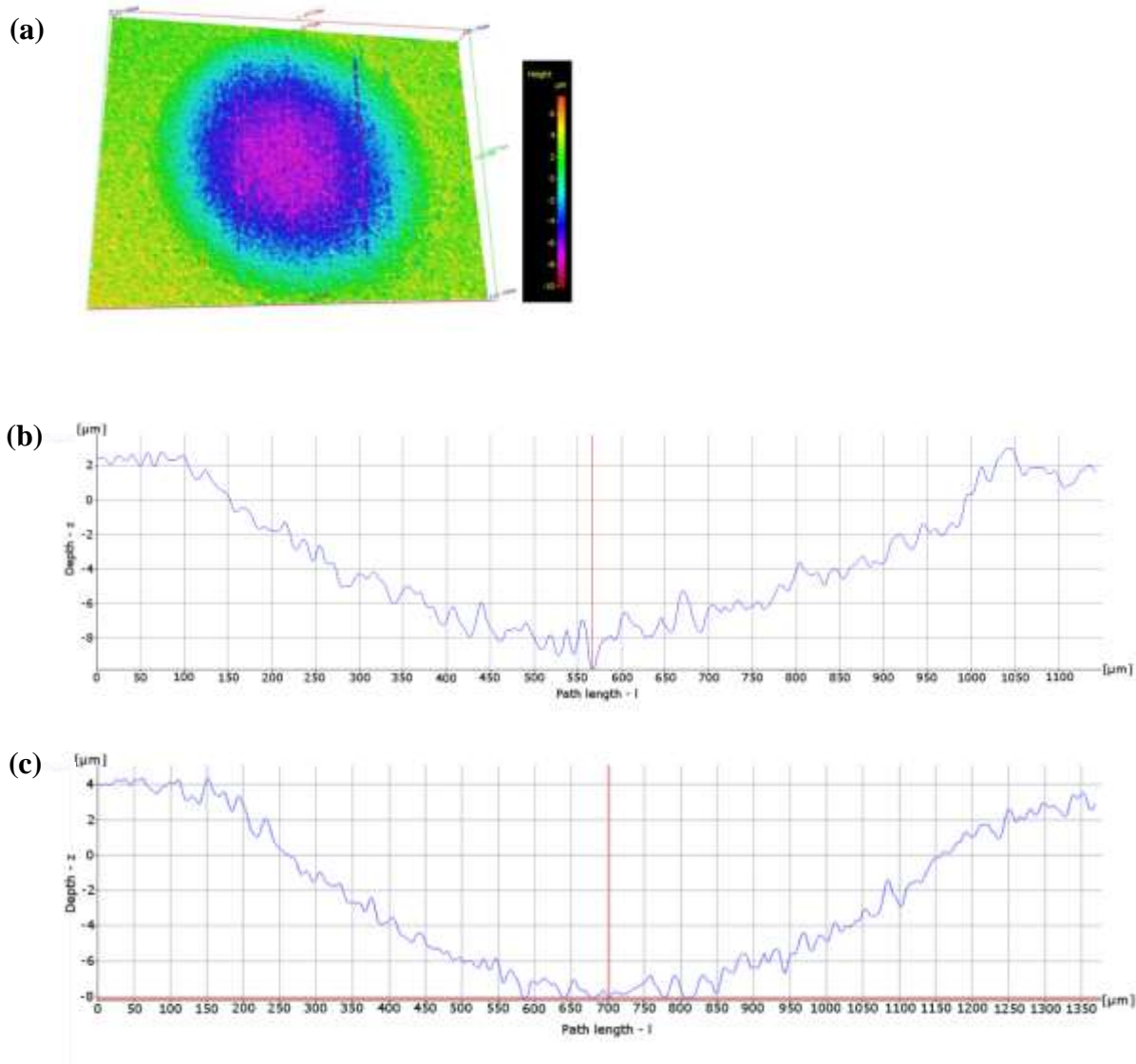
Figure 4: Examination of wear scar (abrasive particles solution) with 3D optical focus-variation microscope (a) 3D optical-variation microscope image for a typical wear scar height contrast map generated during micro-abrasion–corrosion in NaCl and FCS solution in the presence of additional abrasive particles; (b) wear scar profile (particles) indicates deep valleys and peaks towards the centre indicative of 2-body abrasion regime and tending towards shallower peaks towards the crater periphery, indicating a transitioning 3-body regime; (c) wear scar profile (no particles) indicates similar peaks and valleys that appear more uniform across the crater and typical profile of a 2-body abrasion regime.

3.3 Polarisation curves

Fig. 5 shows the polarisation data recorded during micro-abrasion for increasing applied loads in solution with and without particles. As the load increased for the abrasive solution (Fig. 5c) the maximum currents tended to increase. The highest current densities were recorded for 1 and 3N suggesting an increasing corrosion at those loads. In the case of pure NaCl solution (Fig. 5a) E_{corr} appears to have unchanged over the range of applied loads unlike the protein solutions with and without particles. The curves suggest that the surface electrochemical activity is reduced at lower applied loads in the presence and in the absence of abrasive particles. The polarisation curve at 0.5 N applied load for both conditions is observed to remain towards a cathodic potential around –400 mV indicating the lowest electrochemical activity. It is clearly visible as the applied load increased to greater than 0.5 N, the curves tend to shift in the anodic direction as expected. This indicates that the electrochemical activity at the surface increased as the applied load is increased. As the applied load reached 5 N in both cases a sudden cathodic shift is observed. Over the spectrum of applied loads, it appears that electrochemical activity at the contact surface may be enhanced at the higher loading; it is likely that a transition in lubrication mode occurs as a result of changing Hertzian contact pressure which may explain the sudden cathodic shift at 5N. There is good evidence from these results to suggest that the presence of protein in the NaCl solution has an effect on the electrochemical behaviour of CoCrMo during micro-abrasion. The addition of particles appears to enhance the corrosion behaviours; surprisingly, this enhancement is more notable in the solution containing no particles.

(a)

(b)

(c)
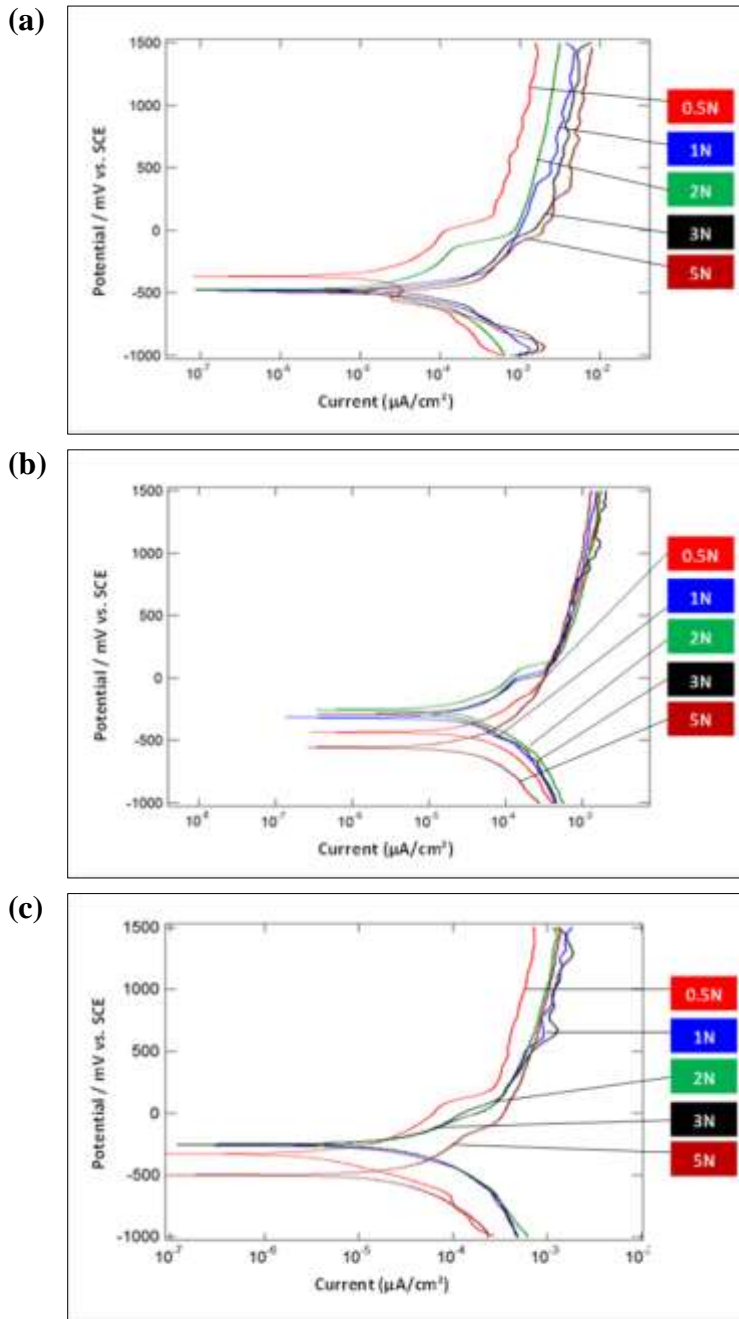
Figure 5: Polarisation curves measured at increasing applied loads for (a) 0.9 % NaCl (b) FCS solution no abrasive particles, and (c) FCS solution with additional abrasive particles

3.4 Potentiostatic measurements

Potentiostatic measurements were also carried out to evaluate the effect of potential and applied load on the corrosion behaviour (Fig. 6). The electrochemical behaviours in solutions with and without particles appear to show similar trends: at lower potentials measured current is generally cathodic dominant as expected from the polarisation curves. Since the alloy surface is not active at cathodic potentials, in this range the current measured is likely due to the reduction of water and dissolved oxygen. As the applied potential is increased there is an increase in current density.

a)

b)

c)

-200 mV

d)

-400 mV

e)
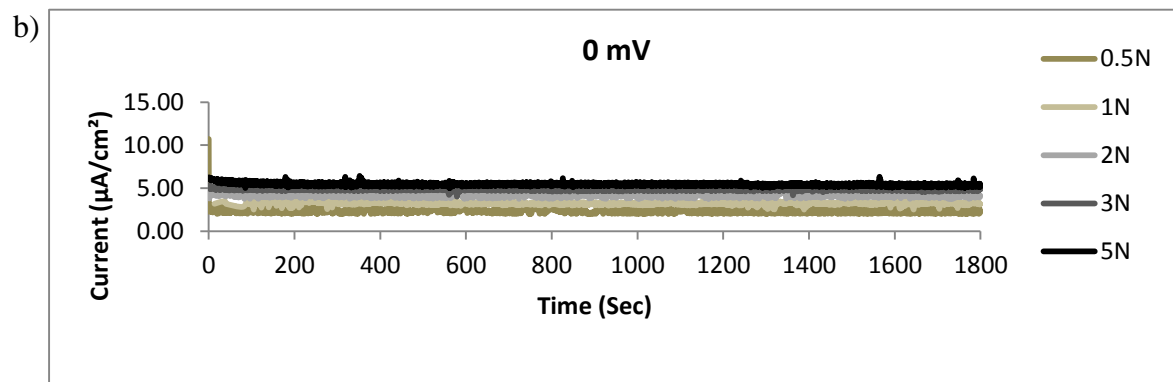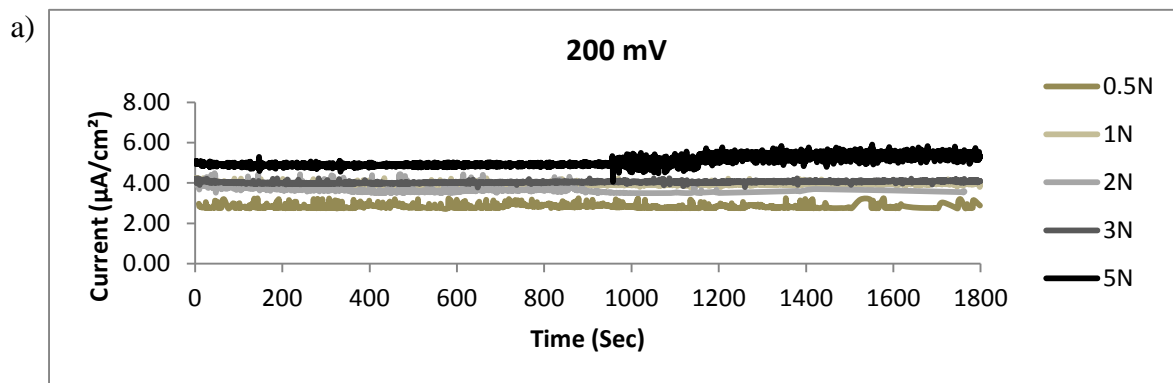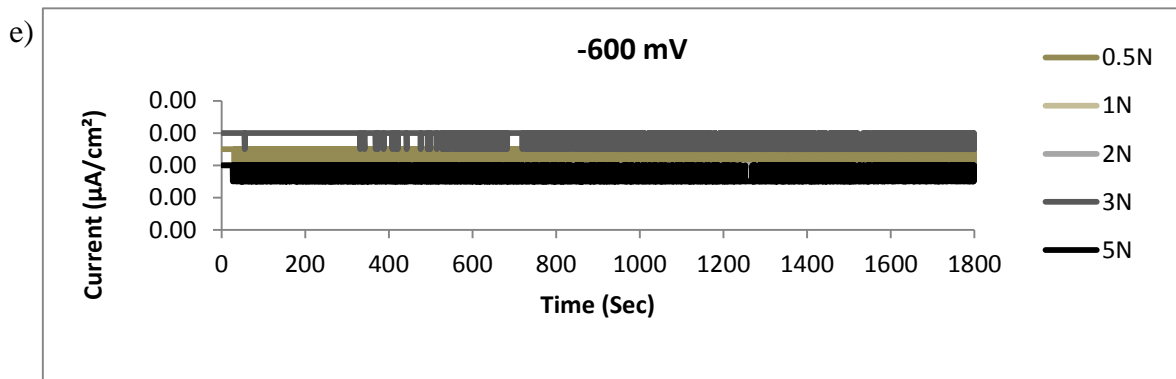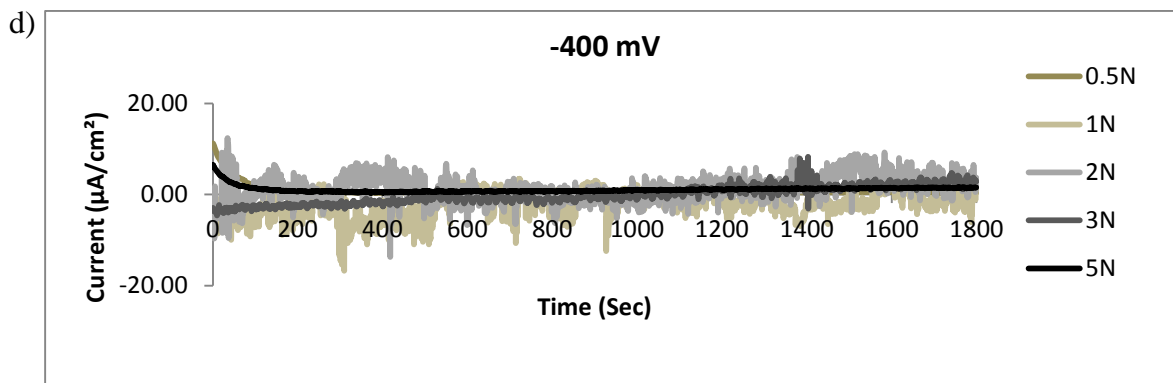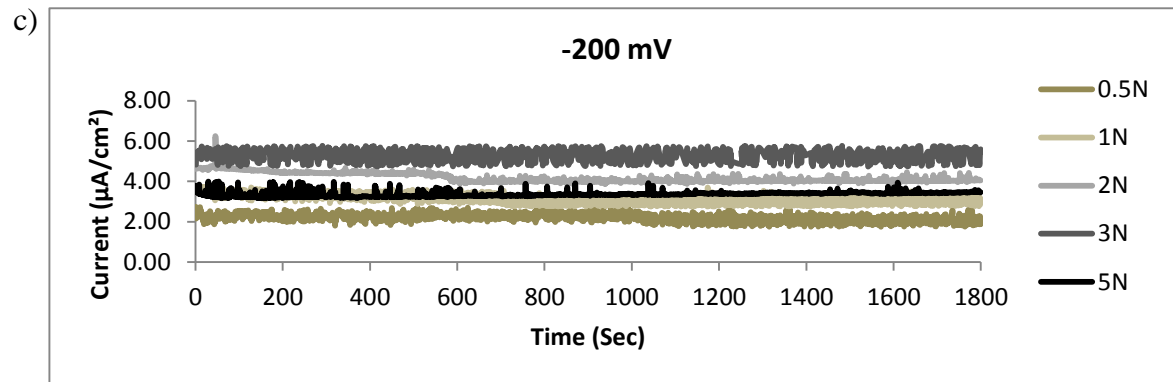
-600 mV

Figure 6: Potentiostatic measurements during micro-abrasion tests at increasing applied potentials and for increasing applied loads: a) 200 mV, b) 0 mV, c) -200 mV, d) -400 mV, e) -600 mV

3.5 Mass loss data

In summary the total mass loss may be represented by its individual mass loss contributions as follows:

$$K_{ac} = K_a + K_c \tag{2}$$

Where K_{ac} (g) represents the total mass of material removed due to micro-abrasion–corrosion; K_a (g) the mass of material removed due to abrasion; and K_c (g) the mass loss due to corrosion.

The mass loss due to abrasion K_a in Eq. 2 may be represented further as:

$$K_a = K_{ao} + \Delta K_a \tag{3}$$

Here K_{ao} represents the mass loss due to abrasion in the absence of corrosion; ΔK_a represents the synergism between corrosion and abrasion, where abrasion is enhanced in the presence of corrosion. When ΔK_a is a negative value it classed as antagonistic. Mass loss due to wear in the absence of corrosion, K_{ao}, was estimated under cathodic conditions at an applied potential of –0.96 V.

Similarly the corrosion mass loss component K_c in Eq. 2 can be represented as:

$$K_c = K_{co} + \Delta K_c \tag{4}$$

Where K_{co} represents the mass loss due to corrosion in the absence of wear; ΔK_c represents the additive effect due to the presence of abrasion in which corrosion is enhanced.

The total mass loss due to micro-abrasion–corrosion may consequently be defined as:

$$K_{ac} = K_{ao} + \Delta K_a + K_{co} + \Delta K_c \tag{5}$$

The mass loss results using this analysis are shown in Table 3. Total mass losses are shown in Fig. 7 for both FCS solution with and without particles. Mass losses due to corrosion K_c and K_{co} were estimated using Faraday's law as follows:

$$K_c = \frac{Q}{ZF} \tag{6}$$

Eq. 6 may also be written as:

$$K_c = \frac{M_w it}{ZF} \tag{7}$$

Where Q is the charge passed (C); F is the Faraday's constant (96,500 C mol^{-1}); z is the number of electrons involved in the corrosion process; i is the total current; t is the exposure time and Mw is the molar mass of the material (g mol^{-1}).

Consistent with Archard's wear model (19), the results indicate a general increased mass loss with applied load. The corrosion mass loss (K_c) appears to have a small contribution to the overall mass loss across the range of loads and potentials tested, and appears to increase with applied potential.

Applied Potential (mV/ SCE)	Applied Load (N)	K_{ac} (µg)	K_c (µg)	K_a (µg)	K_c/ K_a
(a) − 600	0.5	33.25	0.00	33.25	0.00
	1	39.62	0.00	39.62	0.00
	2	69.87	0.00	69.87	0.00
	3	61.08	0.00	61.08	0.00
	5	83.46	0.00	83.46	0.00
(b) − 400	0.5	19.15	0.63	18.52	0.03
	1	26.77	- 1.81	26.77	- 0.07
	2	45.17	- 0.66	45.17	- 0.01
	3	45.17	- 1.72	45.17	- 0.04
	5	59.02	1.32	57.70	0.02
(c) − 200	0.5	16.85	4.47	12.39	0.36
	1	35.98	6.16	29.82	0.21
	2	50.38	7.95	42.43	0.19
	3	57.01	9.94	47.07	0.21
	5	75.82	6.58	69.24	0.10
(d) 0	0.5	17.30	4.61	12.69	0.36
	1	35.28	6.21	29.07	0.21
	2	38.87	8.47	30.40	0.28
	3	51.29	9.48	41.81	0.23
	5	94.53	10.50	84.04	0.12
(e) +200	0.5	11.76	5.78	5.98	0.97
	1	15.54	7.77	7.78	1.00
	2	38.87	7.72	31.14	0.25
	3	31.63	8.05	23.57	0.34
	5	43.53	9.45	34.07	0.28

Table 3: Total mass loss and individual mass loss contributions during micro-abrasion–corrosion of CoCrMo alloy in FCS solution.

Total mass losses (K$_{ac}$) for FCS solution with and without abrasive particles

a)

K$_{ac}$ for applied potential -600 mV

Mass loss (µg)

- □ No particles
- ▨ Particles

Applie load (N)

b)

K$_{ac}$ for applied potential -400 mV

Mass loss (µg)

- □ No particles
- ▨ Particles

Applie load (N)

c)

K$_{ac}$ for applied potential -200 mV

Mass loss (µg)

- □ No particles
- ▨ Particles

Applie load (N)

d)

K$_{ac}$ for applied potential 0 mV

e)

K$_{ac}$ for applied potential +200 mV
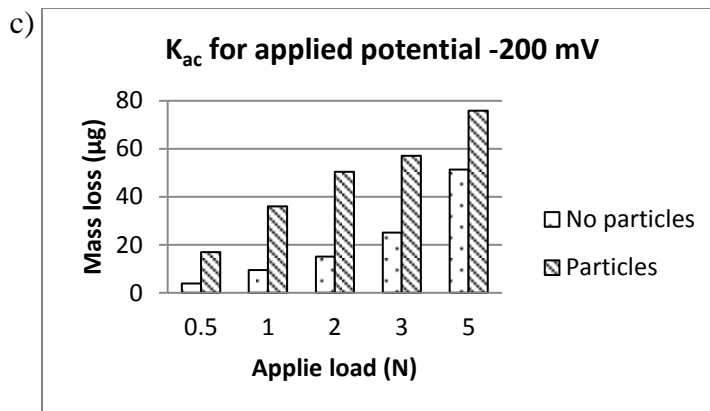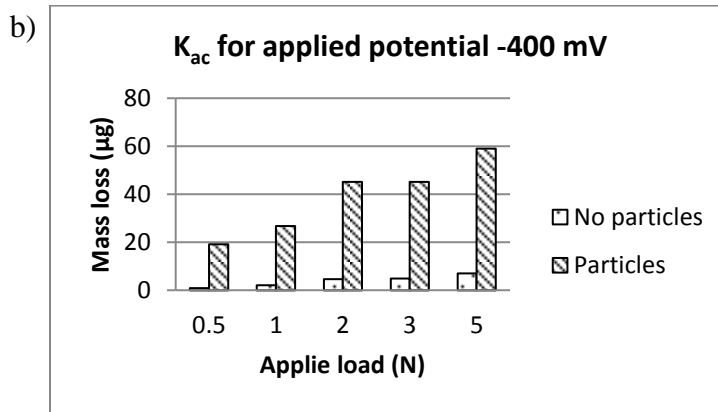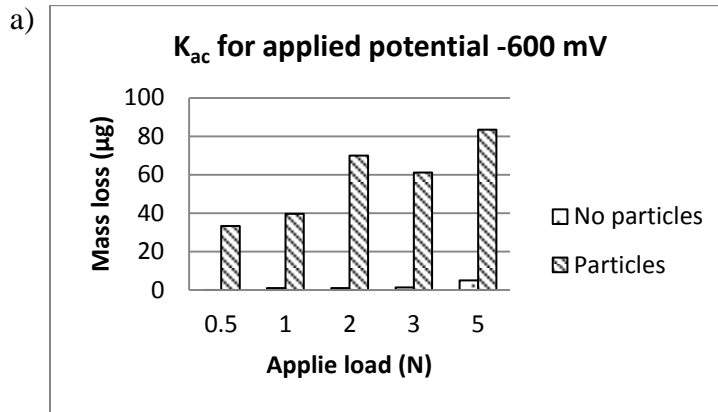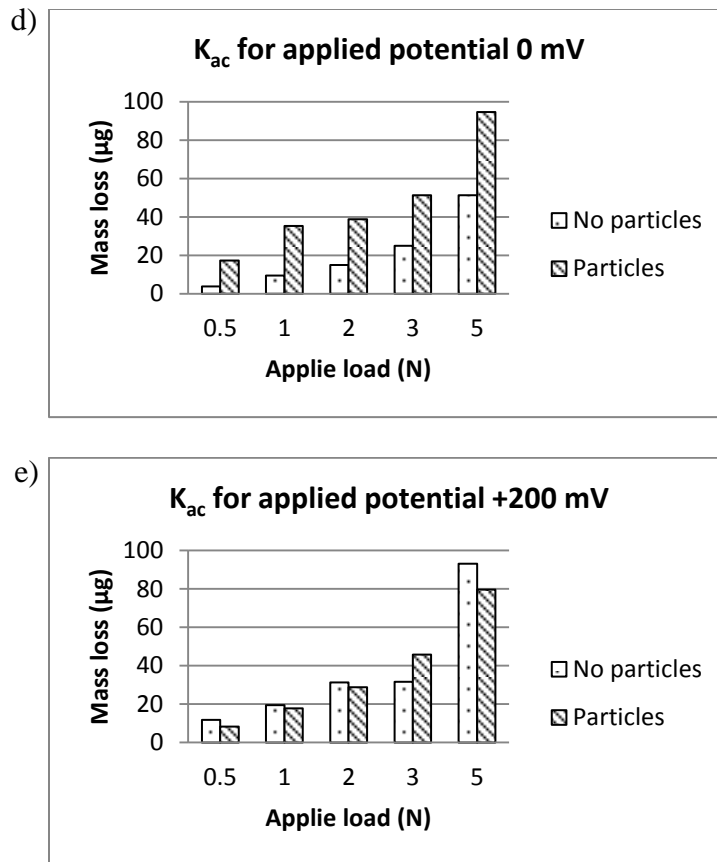
Figure 7: Mass loss comparisons for particles versus no particles. a) to e) increasing applied potential

The experimental error (Fig. 8) was estimated to be ±9% for repeat tests (n = 3) carried out for increasing applied loads and at 0 V applied potential.
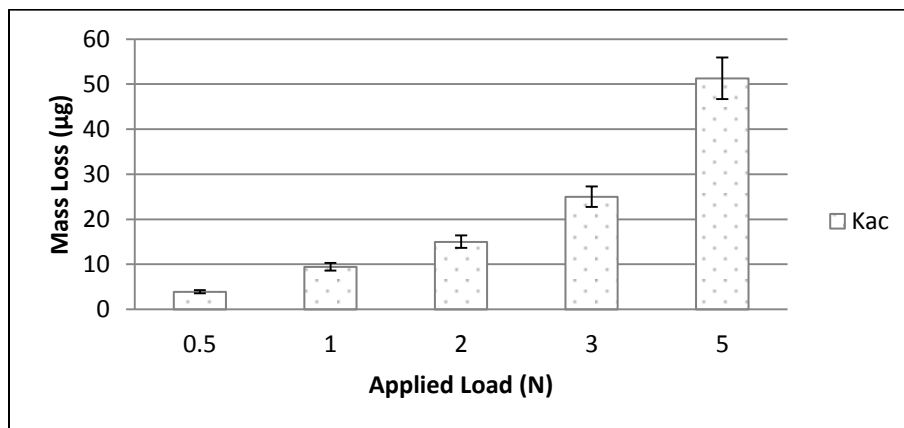
Figure 8: Variation in measured total mass loss (Kac) for increasing applied load at 0 mV applied potential. Repeat tests (n=3) show an error of approximately ±9% measured from images acquired on SEM.

4 Discussion

The purpose of this study was to investigate the tribocorrosion mechanisms of CoCrMo alloy over a range of applied loads and potentials. Tests were performed under idealised hip contact conditions, and in the presence and absence of serum proteins in solution. Loose particles can become trapped at the hip bearing contact (e.g. PMMA in cemented prosthesis, bone fragments), that can intensify the wear–corrosion in-vivo. Micro-abrasion particles were supplemented in the test solution to accelerate and simulate this wear–corrosion process. Furthermore, electrochemical data were recorded over a series of tribocorrosion regimens involving CoCrMo samples, the results of which tests were linked to the abrasion mechanisms following surface analysis. It follows that wear maps may be developed, graphically representing zones and regimes of wear–corrosion over a range of testing parameters. In this way series of wear maps may be developed, in order to describe the fundamental tribocorrosive mechanism in general, and in the context of total hip replacement devices in particular.

4.1 Mass loss behaviour

The polarisation sweeps for FCS solution in the presence, and in the absence of particles (Fig. 5) showed similar trends. It was observed that the measured E_{corr} in both cases shifted anodically as the load was increased. Additionally, potentiostatic tests (Fig. 6) showed an increasing corrosion current as the potential was increased over the range of applied loads, i.e. increasing corrosion in the anodic direction. In non-abrasive particle solution at potentials greater than -200 mV the current appeared to increase less when compared to the lower potential range; this may be explained further by the polarisation

curve indicating a rate limiting corrosion. It was also shown that in this study and previous work (12, 20) the mass loss due to corrosion contributed a small fraction to the overall total mass loss and remained very much independent of applied load.

The mass loss data may be defined using wear–corrosion analysis developed by Yue et al. (21) and following established mass loss analysis methods (22). Generally it is clear that the mass loss (K_{ac}) is consistently higher in solution containing abrasive particles. It can also be seen that mass losses in both solutions tended to increase as applied load was increased; consistent with Archard's wear model (19). As shown in previous work (12, 13) the micro-abrasion (mechanical wear) component contributes a greater part of the total mass loss; the corrosion contribution is small but has been shown to play a critical role in the wear synergism (23). The mass loss contributions to the total mass losses are indicated in Table 3. It can be seen clearly the electrochemical mass loss (K_c) remains consistently fractional towards the total mass loss contribution (K_{ac}). At potentials above 0 mV the mass loss due to corrosion appears to intensify and this trend remains for the increasing potential tests. This would be expected since the alloy surface is more active electrochemically; the increased potential acts to accelerate the surface interaction with its surrounding environment. Since this occurs during a constant sliding, the surface activity is continuously disrupted. The increased electrochemical activity is confirmed on the potentiostatic measurements (Fig. 6) as the potential is increased. At lesser potentials (− 200, − 400 and − 600 mV) the material exhibits lesser electrochemical activity which would be expected as the conditions reach cathodic conditions. Previous work investigating the passivation and trans-passivation behaviour of CoCrMo in simulated

29

physiological solutions (SPS) is well documented (24, 25) including a recently published review article (26). Briefly, it has been shown that the material spontaneously forms a thin Cr rich oxide film on the alloy surface. Hodgson et al. (24) have shown that the film is mainly composed of Cr(III) oxide in the passive region. In the trans-passive region the oxide film composition changes and increases in thickness, also the dissolution rate is increased. The same work has also shown that active dissolution is dominated by the alloying element Co. Therefore in this study it is likely that a passivated (oxide) film was formed at the surface of the alloy in solution. This surface film exhibited a higher stability at lower applied potentials which may explain the E_{corr} behaviour (Fig. 5). Milošev and Strehblow (25) have shown that the composition and thickness of the oxide film in SPS is dependent on the applied potential and exposure time. The same authors, including Hodgson et al., have shown the oxide film is rich in Cr(III) oxide and in smaller amounts Cr(III) hydroxide, a film thickness of up to 3.1 nm at lower potentials (E $\leq$ 0.3 V) has been reported. Mechanical abrasion as a result of the presence of particles may disrupt and remove this film leading to increased corrosion.

Wear mapping

There has been significant developments in describing wear–corrosion interactions in aqueous environments (10, 22, 27, 28); and underlying the concept of micro-abrasion–corrosion (MAC) mapping (12, 13, 20), developed by Stack and co-workers. Several wear maps may be generated based on the results describing wear–corrosion interactions for the conditions tested. A mechanism (or regime) map indicates the dominant mechanism of material wastage. A wastage map indicates the extent of material wastage

(28). Wear–corrosion synergism, an enhanced loss of material due to the combined action of abrasion and corrosion, can similarly be mapped as a function of the testing parameters. The (MAC) mass loss zones or regimes (Table 4) are defined; which follow similar investigations of CoCrMo in which wear maps have been developed (12, 13). In clinical application of wear maps, i.e. implant selection, predicting patient outcomes; relevant wear–corrosion boundaries need to be developed in order to relate clinical factors (i.e. age, weight, activity levels) to wear–corrosion mechanisms. The present work remains at an early stage of development in terms of predicting patient outcomes, focusing instead on fundamental wear mechanisms due to abrasion and corrosion under idealised conditions. Following boundary conditions developed for this study, three categories of MAC maps were constructed: mechanism, wastage and synergy maps. These, along with previously developed wear maps (absence of particles), are shown in Fig. 9.

The wear mapping coordinate axis shows the range of testing parameters; corresponding Hertzian contact pressures are also included. The contact stresses may be calculated from Hertzian equations (29); a maximum Hertzian pressure p_{max} for an applied load of 5 N (initial circular contact radius = 0.34 mm) was calculated at 20.6 MPa.

Map type	Region	Boundaries
Mechanism (Regime)	Micro-abrasion dominated	$\dfrac{K_c}{K_a} \leq 0.1$
	Micro-abrasion– passivation	$0.1 < \dfrac{K_c}{K_a} \leq 1$
	Passivation–micro-abrasion	$1 < \dfrac{K_c}{K_a} \leq 10$
	Passivation-dominated	$\dfrac{K_c}{K_a} > 10$
Wastage	Low	$K_{ac} \leq 30 \times 10^{-6} g$
	Medium	$30 \times 10^{-6} g < K_{ac} \leq 60 \times 10^{-6} g$
	High:	$K_{ac} > 60 \times 10^{-6} g$
Synergy	Additive	$\dfrac{\Delta K_a}{\Delta K_c} \leq 0.1$
	Additive-synergistic	$0.1 < \dfrac{\Delta K_a}{\Delta K_c} \leq 1$
	Synergistic	$\dfrac{\Delta K_a}{\Delta K_c} > 1$

Table 4: Wear map boundary conditions for CoCrMo in FCS solution
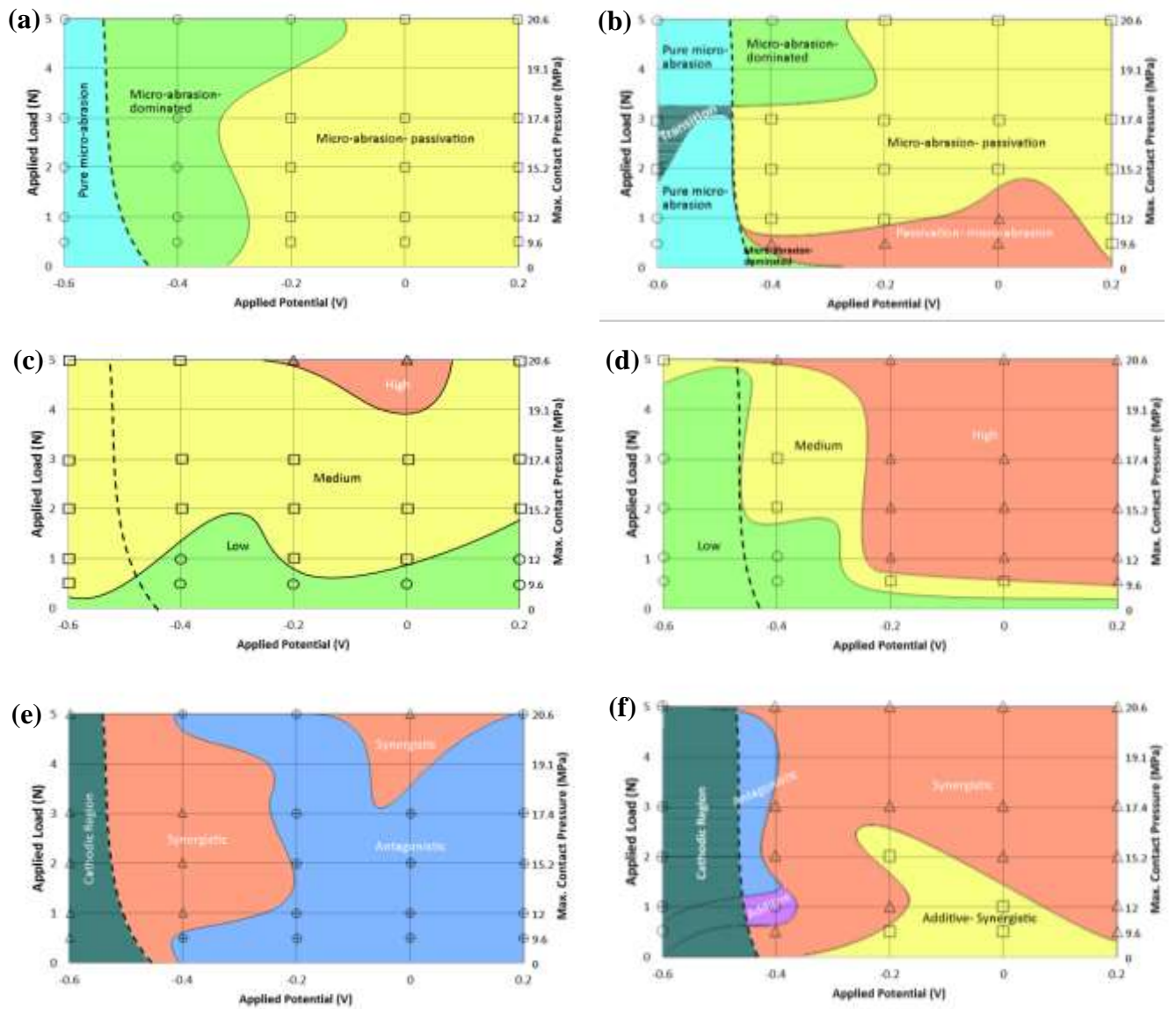
Figure 9: Micro-abrasion–corrosion wear maps for CoCrMo alloy (flat) sliding against a rotating UHMWPE (ball) in FCS solution (pH 7.3, temperature 25°C). Wear maps corresponding to solution containing abrasive SiC particles are arranged down the left column; maps corresponding to no additional particle solution are similarly shown down the right column: (a, b) micro-abrasion–corrosion mechanism maps indicate the mechanism of wear regimes and transition zones over the testing parameters, (c, d) wastage maps define the severity of material loss, (e, f) synergy maps indicate zones of abrasion-corrosion synergy where the volume loss is accelerated due to the combined action of mechanical and chemical interactions; antagonistic zones likely indicate the accumulation of organic material on the alloy surface.

In the presence of particles and at potentials below –300 mV a dominant micro-abrasion regime was identified (Fig. 9a) for the range of increasing applied loads, which suggested that the surface film is more stable and inhibits corrosion over the range of tested potential. Potentials above –300 mV in the abrasive solution indicated a transition to micro-abrasion–passivation dominant regime. In contrast, the solution containing no particles showed a passivation–micro-abrasion regime at low applied loads and peaked at around 0 mV. In terms of synergy effects Sinnett-Jones et al. (30) have found that there are synergistic effects between wear and corrosion ranging from negative to positive (i.e. beneficial to accelerated volume loss rates). The extent of synergy appears to be dependent on the integrity of the passive films and the repassivation kinetics. Mathew et al (23) have also shown that up to 34 % of the total mass loss of CoCrMo is due to synergistic effects in bovine serum during tribocorrosion. In this study the synergy effect was most dominant in the solution containing no particles (Fig. 9f); surprisingly in the presence of particles a dominant antagonism has been observed as shown in the synergy map suggesting improved wear–corrosion.

In this study a 10 vol.% FCS solution was used for the micro-abrasion testing. Proteins in the solution may act as a boundary lubricant and have a beneficial effect on the wear behaviour. Igual Muñoz and Mischler (31) have shown that proteins play a significant role in the electrochemical behaviour of CoCrMo. Similarly Sun et al. (32) studied the effect of protein and pH on CoCrMo during tribocorrosion. The results of that study show that protein adsorption influenced the electrochemical current noise, specific wear rates and the wear scar morphologies during micro-abrasion and was dependent on both the pH

and concentration of protein. In a study conducted by Yan et al. (33) organic species (protein) are shown to enhance the metal ion release in CoCrMo indicating increased corrosion of the surface. Generally, the presence of protein in solution has been shown to form biofilm on the alloy surface and is composed of inorganic graphitic carbon (7). In the present study energy dispersive X-ray analysis was introduced to confirm the presence of protein on the worn contact surface. Fig. 3c shows an EDS spectrum obtained following testing in the FCS solution and additional abrasive particles. In the region close to 0.4 keV a nitrogen peak is observed that is not present on the clean unworn alloy sample surfaces. Similarly a carbon peak is visible at around 0.3 keV, a significantly higher peak intensity following testing when compared to clean unworn surfaces. Given the elemental composition of proteins, it is not unreasonable to expect to see a higher carbon peak intensity following testing in the presence of protein; likewise, the nitrogen peak, which was absent on control samples, confirmed the presence of proteinaceous organic material on those surfaces following testing. The Na and Cl peaks would be expected due to the solution composition of 0.9 % NaCl, the existence of carbon and nitrogen peaks on EDS qualitatively confirms the presence of protein on the wear scar surfaces. Even though the corrosion may be enhanced due to the presence of proteins as reported, the protein-containing fluid plays a critical role in the lubrication at the bearing contact. It has been established that the lubrication is in fact due to graphitic carbon (solid lubricant) that originates from the proteins which can be act to improve wear of the implant surface (7, 18, 23, 34). It is suggested by Wimmer et al. (2001), that in metal-on-metal hip replacements solid layers of protein derived material are likely to be generated between contacting bodies, which may act as solid lubricant separating the bodies.

In more recent work Wimmer et al. (18) studied the microstructural and chemical composition of the contacting surfaces of metal-on-metal implants. They found that nanocrystalline structures form at the implant surface, known as tribolayers. The implant surface layer is transformed to an organic composite material by a process that has been termed mechanical mixing, in which organic species (proteins) are mixed within the metallic surface; but is not yet fully understood. In the present study organic material has been shown to exist on the alloy surface (Fig. 2 and 3) on the wear contact surface and also agglomerated on the surface around the wear scar. The wear map for the abrasive solution indicates a large antagonistic zone. This may be explained possibly due to an increased solution viscosity, improving the lubrication regime and thus inhibiting corrosion-wear due to the mixed protein molecules and particles. In addition hard SiC particles are likely to have embedded on the surface of the softer UHMWPE ball; therefore underlying to a two-body abrasion regime towards the centre of the contact zone (Fig. 2). Loose entrained particles at the outer peripheries of the contact zone led towards a mixed two-body and three-body wear in the presence of particles. It is important to emphasize that the objective of the current work was to demonstrate construction of micro-abrasion–corrosion mapping, relating wear mapping to prosthetic hip replacement bearing materials. Hip contact conditions were idealised for the present investigation. Clearly, more realistic and biomechanically relevant hip contact conditions must be the direction of further wear mapping in this developing area.

5 Conclusions

(i) The effects of applied potential and applied loads were investigated for a CoCrMo alloy in a physiological solution and in the presence of abrasive particles.

(ii) A demonstration of wear maps showed the micro-abrasion–corrosion transitions of CoCrMo in the presence of protein with and without abrasive particles.

(iii) In the presence of abrasive particles wear–corrosion synergy is enhanced at low applied loading in comparison to the same test conditions in the absence of particles.

(iv) As part of a progressive understanding of the wear behaviour of such implant material, the interaction of proteins and surface oxide/ protein layer will be investigated using surface analysis techniques including AFM and SEM.

(v) The results indicated that proteins present in foetal calf serum solution may result in the development of a graphitic tribo-layer; and play a critical role in enhancing or protecting against tribo-corrosive degradation.

REFERENCES

1.   NJR. 9th Annual Report. 2012.

2.   Affatato S, Spinelli M, Zavalloni M, Mazzega-Fabbro C, Viceconti M. Tribology and total hip joint replacement: Current concepts in mechanical simulation. Medical Engineering & Physics. 2008;30(10):1305-17.

3.   H. Bhatt, Goswami T. Implant wear mechanisms–basic approach. Biomedical materials (Bristol, England). 2008;3(4):042001.

4.   Mathew MT, Srinivasa Pai P, Pourzal R, Fischer A, Wimmer MA. Significance of Tribocorrosion in Biomedical Applications: Overview and Current Status. Advances in Tribology. 2009;2009.

5.   Landolt D, Mischler S, Stemp M. Electrochemical methods in tribocorrosion: a critical appraisal. Electrochimica Acta. 2001;46(24–25):3913-29.

6.   Buford A, Goswami T. Review of wear mechanisms in hip implants: Paper I – General. Materials & Design. 2004;25(5):385-93.

7.   Liao Y, Hoffman E, Wimmer M, Fischer A, Jacobs J, Marks L. CoCrMo metal-on-metal hip replacements. Physical Chemistry Chemical Physics. 2013;15(3):746-56.

8.   Mischler S, Muñoz AI. Wear of CoCrMo alloys used in metal-on-metal hip joints: A tribocorrosion appraisal. Wear. 2013;297(1–2):1081-94.

9.   M.H. Stephen, C.S. Ming, Wear Maps. Modern Tribology Handbook, Two Volume Set. Mechanics & Materials Science: CRC Press; 2000.

10.   Stack MM. Mapping tribo-corrosion processes in dry and in aqueous conditions: some new directions for the new millennium. Tribology International. 2002;35(10):681-9.

11.   Lim SC, Ashby MF. Wear-Mechanism maps. Acta Metallurgica. 1987;35(1):1-24.

12.   Stack MM, Rodling J, Mathew MT, Jawan H, Huang W, Park G, et al. Micro-abrasion–corrosion of a Co–Cr/UHMWPE couple in Ringer's solution: An approach to construction of mechanism and synergism maps for application to bio-implants. Wear. 2010;269(5–6):376-82.

13.   Sadiq K, Black RA, Stack MM. Bio-tribocorrosion mechanisms in orthopaedic devices: Mapping the micro-abrasion-corrosion behaviour of a simulated CoCrMo hip replacement in calf serum solution. Wear. 2014;316(1-2):58-69.

14.   Amini S, Miserez A. Wear and abrasion resistance selection maps of biological materials. Acta Biomaterialia. 2013;9(8):7895-907.

15.   Gant AJ, Gee MG. A review of micro-scale abrasion testing. Journal of Physics D: Applied Physics. 2011;44(7):073001.

16.   Adachi K, Hutchings IM. Wear-mode mapping for the micro-scale abrasion test. Wear. 2003;255(1–6):23-9.

17.   Stack MM, Mathew M. Micro-abrasion transitions of metallic materials. Wear. 2003;255(1–6):14-22.

18.   Wimmer MA, Fischer A, Buscher R, Pourzal R, Sprecher C, Hauert R, et al. Wear mechanisms in metal-on-metal bearings: the importance of tribochemical reaction layers. J Orthop Res. 2010;28(4):436-43.

19.   Archard JF. Contact and Rubbing of Flat Surfaces. Journal of Applied Physics. 1953;24(8):981-8.

20.   Stack MM, Jawan H, Mathew MT. On the construction of micro-abrasion maps for a steel/polymer couple in corrosive environments. Tribology International. 2005;38(9):848-56.

21.   Z. Yue, P. Zhou, J. Shi, editors. Some factors influencing erosion–corrosion performance of materials: ASME; 1987.

22.   Stack MM, Chi K. Mapping sliding wear of steels in aqueous conditions. Wear. 2003;255(1–6):456-65.

23.   Mathew MT, Jacobs JJ, Wimmer MA. Wear-corrosion synergism in a CoCrMo hip bearing alloy is influenced by proteins. Clinical orthopaedics and related research. 2012;470(11):3109-17.

24.   Hodgson AWE, Kurz S, Virtanen S, Fervel V, Olsson COA, Mischler S. Passive and transpassive behaviour of CoCrMo in simulated biological solutions. Electrochimica Acta. 2004;49(13):2167-78.

25.   Milošev I, Strehblow HH. The composition of the surface passive film formed on CoCrMo alloy in simulated physiological solution. Electrochimica Acta. 2003;48(19):2767-74.

26.   Pound BG. Passive films on metallic biomaterials under simulated physiological conditions. Journal of Biomedical Materials Research Part A. 2014;102(5):1595-604.

27.   Jiang J, Stack MM, Neville A. Modelling the tribo-corrosion interaction in aqueous sliding conditions. Tribology International. 2002;35(10):669-79.

28.   Stack MM, Jana BD, Abdelrahman SM. Models and mechanisms of erosion-corrosion in metals. In: Landolt D, Mischler S, editors. Tribocorrosion of Passive Metals and Coatings. Cambridge: Woodhead Publishing Ltd.; 2011.

29.   G. Stachowiak, A.W. Batchelor, Engineering Tribology: Butterworth-Heinemann; 2011.

30.   Sinnett-Jones PE, Wharton JA, Wood RJK. Micro-abrasion–corrosion of a CoCrMo alloy in simulated artificial hip joint environments. Wear. 2005;259(7–12):898-909.

31.   Muñoz AI, Mischler S. Interactive Effects of Albumin and Phosphate Ions on the Corrosion of CoCrMo Implant Alloy. Journal of The Electrochemical Society. 2007;154(10):C562-C70.

32.   D. Sun, J.A. Wharton, R.J.K Wood, The Effects of Protein and pH on the Tribo-Corrosion Performance of Cast CoCrMo – A Combined Electrochemical and Tribological Study. Advanced Tribology2009. p. 825-6.

33.   Yan Y, Neville A, Dowson D. Biotribocorrosion of CoCrMo orthopaedic implant materials—Assessing the formation and effect of the biofilm. Tribology International. 2007;40(10–12):1492-9.

34.   Liao Y, Pourzal R, Wimmer MA, Jacobs JJ, Fischer A, Marks LD. Graphitic tribological layers in metal-on-metal hip replacements. Science. 2011;334(6063):1687-90.

35.   Wimmer MA, Loos J, Nassutt R, Heitkemper M, Fischer A. The acting wear mechanisms on metal-on-metal hip joint bearings: in vitro results. Wear. 2001;250(1–12):129-39.

TABLES

FIGURE LIST